Monthly Notices of the ROYAL ASTRONOMICAL SOCIETY

MNRAS **505,** 4106–4119 (2021)
Advance Access publication 2021 June 7

https://doi.org/10.1093/mnras/stab1594

Modelling of SN 2013dx associated with the low-redshift GRB130702A points to diversity in GRB/SN properties

P. A. Mazzali,[1,2]★ E. Pian,[1,3] F. Bufano[4] and C. Ashall[5]

[1]*Astrophysics Research Institute, Liverpool John Moores University, IC2, Liverpool Science Park, 146 Brownlow Hill, Liverpool L3 5RF, UK*
[2]*Max-Planck-Institut für Astrophysik, Karl-Schwarzschild Str 1, D-85748 Garching, Germany*
[3]*INAF, Astrophysics and Space Science Observatory, Via P. Gobetti 101, I-40129 Bologna, Italy*
[4]*INAF, Astrophysical Observatory of Catania, Via Santa Sofia 78, I-95123 Catania, Italy*
[5]*Institute for Astronomy, University of Hawai'i at Manoa, 2680 Woodlawn Drive, Hawai'i, HI 96822, USA*

Accepted 2021 May 27. Received 2021 May 27; in original form 2021 March 16

ABSTRACT

The properties of the broad-lined Type Ic supernova (SN) 2013dx, associated with the long gamma-ray burst GRB 130702A at a redshift $z = 0.145$, are derived via spectral modelling. SN 2013dx was similar in luminosity to other GRB/SNe, with a derived value of the mass of ^{56}Ni ejected in the explosion of $\approx$0.4 M$_\odot$. However, its spectral properties suggest a smaller explosion kinetic energy. Radiation transport models were used to derive a plausible mass and density distribution of the SN ejecta in a one-dimensional approximation. While the mass ejected in the explosion that is obtained from the modelling ($M_{\rm ej} \approx 9$ M$_\odot$) is similar to that of all other well-studied GRB/SNe, the kinetic energy is significantly smaller ($E_{\rm K} \sim 10^{52}$ erg). This leads to a smaller $E_{\rm K}/M_{\rm ej}$ ratio, $\approx 10^{51}$ erg/M$_\odot$, which is reflected in the narrower appearance of the spectral lines. While the low $E_{\rm K}$ does not represent a problem for the scenario in which magnetar energy aids powering the explosion and the nucleosynthesis, it is nevertheless highly unusual. SNe Ic with similar $E_{\rm K}$ have never been seen in coincidence with a GRB, and no well-observed GRB/SN has shown similarly low $E_{\rm K}$ and $E_{\rm K}/M_{\rm ej}$.

Key words: radiative transfer – techniques: spectroscopic – supernovae: general – supernovae: individual SN 2013dx.

1 INTRODUCTION

Although long-duration gamma-ray bursts (GRBs) are relatively common events ($\sim$1 d^{-1}), only rarely, roughly once per year or less, do they happen close enough to the Earth that we can study the stellar death that accompanies them in any detail (Galama et al. 1998; Hjorth et al. 2003; Levan et al. 2016).

The understanding of the significance of the broad-lined spectra that are so characteristic of the Type Ic supernovae (SNe) that typically accompany GRBs[1] led to the realization that GRB/SNe are extremely energetic explosions (Iwamoto et al. 1998; Mazzali, Iwamoto & Nomoto 2000), where material from the carbon–oxygen core of the progenitor star is ejected with kinetic energies ($E_{\rm K}$) of several 10^{52} erg, i.e. more than an order of magnitude larger than the so-called typical SN energy. In fact, the prototypical GRB/SN 1998bw had an $E_{\rm K}$ as high as 4×10^{52} erg in spherical symmetry (Iwamoto et al. 1998), and other events that have been carefully analysed have yielded similar values, from SN 2003dh (3×10^{52} erg; Mazzali et al. 2003) to SN 2003lw (5×10^{52} erg; Mazzali et al. 2006a), and SN 2016jca (4×10^{52} erg; Ashall et al. 2019).

The extremely high $E_{\rm K}$ is invariably accompanied by a rather large ejected mass $M_{\rm ej} \sim 10$ M$_\odot$, and a high luminosity, which is the result of the synthesis and radioactive decay of several tenths of a $M_\odot$ of ^{56}Ni, again an unusually high value for core-collapse SNe (GRB/SNe produce almost as much ^{56}Ni as SNe Ia). As GRB/SNe are all of Type Ic (with the possible exception of the Type Ib SN 2008D, which was accompanied by an X-ray flash, Mazzali et al. 2008a; Soderberg et al. 2008; Modjaz et al. 2009; Tanaka et al. 2009), the ejected mass typically reflects the mass of the carbon–oxygen core of the progenitor star, which scales roughly with the mass of the star at birth. Such relations (e.g. Nomoto & Hashimoto 1988) suggest progenitor zero-age main-sequence masses of $\sim$35–50 M$_\odot$. It is therefore natural to hypothesize that the large mass of these core-collapse events is in some way responsible for the large $E_{\rm K}$, or, at least, that it is one of the driving factors. How this may exactly happen is not clear, however, as it is very unlikely that neutrinos can deposit so much of their energy to the stellar envelope (Janka, Melson & Summa 2016). One current hypothesis is that energy is extracted from a highly rotating, magnetized proto-neutron star (proto-NS) (a magnetar) that forms upon the collapse of the core (Bucciantini et al. 2009; Metzger et al. 2015). Given the high mass of the progenitors, it is more likely that the final result of the collapse is a black hole, but a temporary NS phase may not be excluded, especially if the compact object is born with a high rotation rate. A magnetar can store up to $\sim 2.5 \times 10^{52}$ erg of rotational energy, which is sufficient to power every GRB/SN if we assumed that the isotropic $E_{\rm K}$ derived from modelling on-axis events is overestimated by a factor of 2–3 as a consequence of the asphericity of the ejecta, which would be a natural consequence of the magnetic field configuration (Uzdensky & MacFadyen 2007) and our privileged viewing angle

★ E-mail: mazzali@MPA-Garching.MPG.DE

[1]Type Ic SNe are core-collapse events of stars stripped of their outer H and He layers. See Filippenko (1997) for a spectral classification of SNe.

© 2021 The Author(s)
Published by Oxford University Press on behalf of Royal Astronomical Society

Downloaded from https://academic.oup.com/mnras/article/505/3/4106/6294487 by Liverpool John Moores University user on 01 November 2022

(Maeda et al. 2002; Mazzali et al. 2005). How the energy is extracted is again unclear. What is clear is that the energy must be extracted very quickly, in a matter of a second or less, in order to power the explosion and lead to the synthesis of large amounts of ^{56}Ni (Suwa & Tominaga 2015; Chen et al. 2017). Although it is sometimes suggested that the long-term decay of the magnetar can power the SN light curve (e.g. Kasen & Bildsten 2010; Woosley 2010), this is not necessary for a GRB/SN, since we know from nebular data (Mazzali et al. 2001b, 2007; Maeda et al. 2007) that the radioactive decay of ^{56}Ni can power both the light curve and the nebular epoch emission, which is dominated by lines of oxygen and iron. In the case of GRB/SNe, magnetic energy could energize the explosion, leading to the observed near-constant explosion kinetic energy (Mazzali et al. 2014), and possibly contribute to the synthesis of ^{56}Ni.

As the field is awaiting a theoretical breakthrough, the study and analysis of individual events is certainly a worthwhile effort, both to confirm the trend and to identify exceptions, should any be found, which may light the path to answering to the questions presented above.

The case of SN 2013dx is an intriguing one. The SN was associated with GRB 130702A, a rather normal long GRB (Singer et al. 2013; D'Elia et al. 2015; Toy et al. 2016). The SN was as luminous as other GRB/SNe, and its spectrum showed broad lines (D'Elia et al. 2015), but at a closer look line blending was not quite as extreme as in textbook cases such as SN 1998bw. We know that line blending is a proxy for $E_{\rm K}$ (Mazzali et al. 2017). Prentice & Mazzali (2018) introduced a simple method to estimate the relative $E_{\rm K}$ of SNe Ic using a count of the number of spectral features in the optical spectral range near maximum: GRB/SNe show typically three features and are classified as Ic-3. SN 2013dx, on the other hand, showed four features, with the Fe-dominated absorption at 4000–5000 Å split into two components, and quite possibly also the Ca II IR triplet not blending with the (weak) O I 7774 line, which suggests that the amount of material moving with $v > 0.1c$ was significantly smaller than that in other GRB/SNe. Therefore, while most previously studied GRB/SNe required only a small change to the original model that was used to match SN 1998bw, SN 2013dx offers the opportunity to explore a different range of parameters and to apply the experience we have gained from modelling both GRB/SNe and other broad-lined SNe Ic that did not show an accompanying GRB (e.g. Mazzali et al. 2013, 2017).

In this paper, we analyse the spectra first presented by D'Elia et al. (2015) and present a new spectrum taken with the ESO VLT about 6 months after explosion, when the SN was expected to be in the nebular phase. The data have been newly decomposed, as discussed in Section 2. Spectral models were computed using our well-established Monte Carlo radiation transport code for SNe. As discussed in Section 3, different explosion models were used in order to determine as accurately as possible the values of $M_{\rm ej}$ and $E_{\rm K}$. Lacking reliable nebular data, we were forced to constrain the ^{56}Ni mass using only a combination of the abundances derived from the early-time modelling and a light-curve simulation. This was done using our Monte Carlo light-curve code and is discussed in Section 4. Having obtained a reasonable result from modelling, we discuss its possible significance in Section 5 and conclude in Section 6.

2 REVISED DECOMPOSITION OF SPECTRA AND LIGHT CURVES

In this section, we present an updated decomposition of the optical counterpart of GRB130702A into host galaxy, afterglow, and SN contributions. This improves on previous attempts by taking into account a larger data set and an accurate method for afterglow modelling (Ashall et al. 2019). Although all available optical photometry is used (Singer et al. 2013; D'Elia et al. 2015; Toy et al. 2016), our SN spectral analysis relies only on the VLT+FORS spectra (D'Elia et al. 2015), which have the best signal-to-noise ratio.

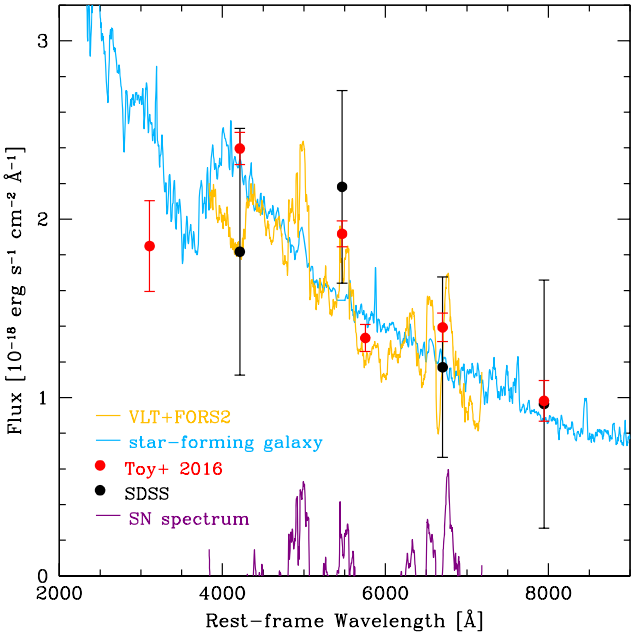

Figure 1. VLT + FORS2 spectrum taken in 2014 January–March (yellow), cleaned of spurious features, corrected for redshift ($z = 0.145$), Galactic absorption [$E(B-V) = 0.037$ mag], smoothed with a boxcar of 50 Å, and scaled to match the late-epoch flux measurements made with Keck in the *ugriz* filters (red circles, from Toy et al. 2016). The SDSS *ugriz* photometry of the host galaxy is also shown (black circles). The template of a star-forming galaxy with low intrinsic extinction [$E(B-V) < 0.1$ mag], from Kinney et al. (1996), is shown for comparison (light blue). The violet curve is the residual SN spectral signal obtained after subtracting the star-forming template spectrum from the VLT spectrum. No identifiable nebular emission lines are seen, notably [O I] 6300,6363.

2.1 Late-epoch spectrum and host galaxy

Late-epoch spectroscopic exposures with the VLT and FORS2 equipped with grism 300V+GG435 were taken on 2014 January 22 (2 × 1800 s), March 11 (2 × 1800 s), and March 13 (4 × 1800 s), i.e. 178, 220, and 222 rest-frame days after explosion, respectively, in order to search for emission lines, the strongest spectral signature expected from the SN in the nebular phase. The spectra were reduced with standard methods. No nebular emission lines appear to be superposed on to the continuum, which is dominated by the flux of the host galaxy, as shown in Fig. 1. In this figure, we show the co-added VLT spectrum scaled in flux to match the late-epoch photometry taken at 330 and 632 d after explosion (Toy et al. 2016) and compare it to SDSS photometry and to the template of a little-extinguished star-forming galaxy (Kinney et al. 1996; see also Kelly et al. 2013).

The spectra are generally consistent with the photometry, with the exception of the SDSS points at ∼4000 and 5500 Å, which have, however, large errors. The VLT spectrum thus represents exclusively the host galaxy. However, owing to its poor quality and limited wavelength extension, we preferred to use the low-extinction star-forming template for subtraction of the host galaxy contribution from all spectra in our study. This choice is justified by the fact

Downloaded from https://academic.oup.com/mnras/article/505/3/4106/6294487 by Liverpool John Moores University user on 01 November 2022

that long GRBs are known to be generally hosted by galaxies with high star formation rate and in this specific GRB, there is no evidence of significant intrinsic extinction. For the near-infrared (NIR) photometry, we extrapolated the template spectrum to longer wavelengths using a power law.

2.2 Multiwavelength afterglow

In order to isolate the SN component, previous authors estimated the afterglow contribution assuming that it is produced by synchrotron radiation in a relativistic shock that interacts with a uniform external medium, as prescribed by the classical fireball model ($f(t) \propto t^{-\alpha}\nu^{-\beta}$, Zhang & Mészáros 2004; Racusin et al. 2009, and references therein). The energy distribution of the relativistic particles follows a power law of the form $dN/dE \propto E^{-p}$. The characteristic frequency of the particles that lose a substantial fraction of their energy to synchrotron radiation (cooling frequency) is indicated with ν_c.

While D'Elia et al. (2015) limited their analysis to the optical light curve, Singer et al. (2013) and Toy et al. (2016) considered also the *Neil Gehrels Swift Observatory* (*Swift*) X-ray Telescope (XRT) light curve (0.3–10 keV) and tried a simultaneous fit of both X-ray and optical data within the above model. However, they did not take into account the first *r*-band photometric point and the afterglow decay prior to the time break that they measure to occur at 1.17 d.

Here, we propose a model of the optical and X-ray afterglow of GRB130702A based on classical fireball theory that consistently takes into account the observed spectral slopes, decay indices, and *r*-band light-curve steepening. In doing so, we adopted the same approach used in the case of the multiwavelength afterglow of GRB161219B (Ashall et al. 2019), which required the injection of a refreshed blast wave starting within a few hours of the main GRB event, and used that same formalism to evaluate the model parameters.

We downloaded from the *Swift* archive the most up-to-date XRT light curve of GRB130702A, which extends to more than 100 d after explosion (https://www.swift.ac.uk/xrt_curves/00032876/). This is consistent with a single power law of index $\alpha = 1.21 \pm 0.02$. The X-ray spectrum, de-absorbed for a Galactic $N_{\rm HI} = 1.83 \times 10^{20}$ cm^{-2} and a poorly constrained intrinsic $N_{\rm HI} \simeq 6 \times 10^{20}$ cm^{-2}, is well fitted by a single power law with photon index $\Gamma = \beta_X + 1 = 1.82 \pm 0.12$ (http://www.swift.ac.uk/xrt_spectra/00032876/). The optical spectrum taken ∼1 d after explosion was corrected for Galactic ($A_{\rm V} = 0.116$ mag, Schlafly & Finkbeiner 2011) as well as intrinsic absorption ($A_{\rm V} = 0.10$ mag, Toy et al. 2016). It can then be represented by a single power law with $\beta_{\rm opt} = 0.52 \pm 0.19$ (Toy et al. 2016). This is flatter than the X-ray spectral slope, although still marginally consistent with it. The optical light curves (except in the *r*-band) were monitored starting ∼1 d after explosion. They decay as single power laws with index $\alpha \simeq 1.1$–1.2 between day 1 and day 4 (Singer et al. 2013; Toy et al. 2016). The *r*-band light curve, which was monitored starting ∼4 h after explosion, cannot be described by a single power law. It requires a broken power law with an early decay of $\alpha = 0.57$ and a steepening after a few days (Singer et al. 2013; Toy et al. 2016), which appears to be larger ($\Delta\alpha \approx 0.7$) than a cooling break ($\Delta\alpha = 0.25$). At epochs later than 4 d, all optical light curves exhibit an extra component, which has been interpreted as the emergence of SN light (Singer et al. 2013; D'Elia et al. 2015; Toy et al. 2016; Volnova et al. 2017).

If the *r*-band light-curve steepening observed a few days after explosion is due to jet geometry and the consequent coming into view of the side of the jet, it must occur achromatically. According to fireball theory, if $p = 2.64$ as derived from $\beta_{\rm X}$ assuming that $\nu_{\rm X} < \nu_c$, the X-ray light curve (which is unaffected by the SN light) should decay as $t^{-2.64}$ after the break, which is inconsistent with the *Swift*/XRT data. A fit to the X-ray light curve with a broken power law cannot reproduce a post-break $t^{-2.64}$ decay for any value of the break time. Therefore, we assume hereafter $\nu_{\rm X} > \nu_c$, which appears also more realistic (it is unlikely that ν_c is larger than the X-ray frequency at a few days after explosion).

If $\nu_{\rm X} > \nu_c$, $p = 2\beta_{\rm X} = 1.64$, i.e. $p < 2$, which in principle requires that we adopt the parameter dependencies that are appropriate for a 'flat' electron–energy law (Dai & Cheng 2001; Zhang & Mészáros 2004). However, the $p < 2$ fireball prescription for frequencies larger than ν_c does not yield a good fit to the X-ray light curve: the time indices before and after the break are too steep for any break between 1 and a few days. We then resorted to the hypothesis and formalism developed in Ashall et al. (2019): although formally the electron–energy law is highly energetic ($p < 2$), which causes rapid cooling and therefore steep decay indices, the external shock that produced the afterglow is not an impulsive blast but is refreshed a few hours after the explosion, so that the added energy slows down the decay rates. Under this assumption, we used $p = 1.64$, but applied to the X-ray and optical afterglow the closure relations that are appropriate for the case $p > 2$ (Zhang & Mészáros 2004).

The multiwavelength light curves, corrected for Galactic and intrinsic extinction and *k*-corrected using the XRT and VLT spectra, are shown in Fig. 2, left-hand panel, before and after host galaxy and afterglow subtraction, and with model curves. In Fig. 2, right-hand panel, we reported only the subtracted SN curves in the optical and NIR bands where the SN signal is significant. The simultaneous best fit of the X-ray and all optical light curves, carried out via a χ^2-minimization routine, is obtained for a time break of ≈3 d. The model X-ray decay index before the time break, $\alpha_{\rm X} = 0.73$, is apparently too steep for the optical *r*-band light curve, which suggests that ν_c is located between the optical and X-ray domain (the best-fitting value at 1 d is $\nu_c = 1.5 \times 10^{15}$ Hz). This is also consistent with the slope of the optical spectrum ($\beta_{\rm opt} \sim 0.5$) determined by Toy et al. (2016).

If the extra luminosity input required by our approach is modelled as $L(t) \propto t^{-q}$, the q parameter can be derived as in Ashall et al. (2019, see their appendix) to be $q \simeq 0.84$, which is very similar to that determined by Ashall et al. (2019) for GRB161219B, and conveniently smaller than 1, so that the integrated luminosity increases with time and efficiently re-energizes the shock until a cutoff is reached.

2.3 Supernova component

By subtracting the host galaxy and the afterglow contributions from the observed optical light curves, we obtained the SN light curves (shown in lighter tones in Fig. 2). We used the monochromatic light curves in which the SN was best detected and monitored to construct a rest-frame pseudo-bolometric light curve in the range of 4500–10 500 Å. In order to do this, we interpolated the *g, r, i, z, y* fluxes at intervals of 1 d, integrated the resulting spectral flux distribution over the corresponding wavelength range (4825–10 200 Å), added flux shortwards and longwards of the wavelength boundaries of this range to 4500 and 10 500 Å, respectively, by assuming a flat flux power law with respect to wavelength, and remapped it to the exact epochs of observation. We then computed the pseudo-bolometric luminosity using $z = 0.145$ and assuming $H_0 = 73$ km s^{-1} Mpc^{-1} (Riess et al. 2016) and a concordant cosmology. This is shown in Fig. 3.

The curve shape and luminosity are consistent with those published by D'Elia et al. (2015) and Toy et al. (2016), considering the different

Downloaded from https://academic.oup.com/mnras/article/505/3/4106/6294487 by Liverpool John Moores University user on 01 November 2022

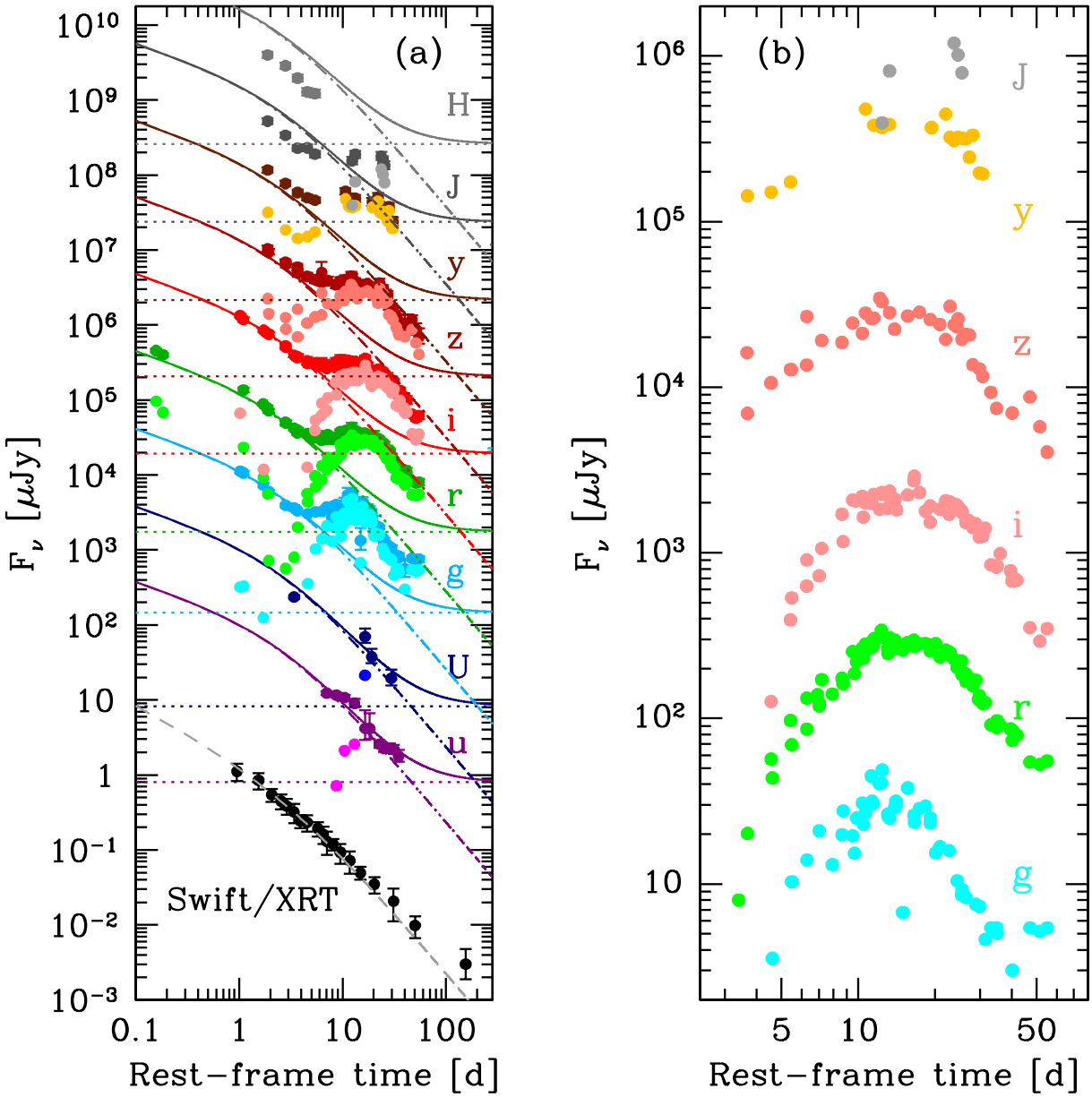

Figure 2. (a) Multiwavelength light curves of the GRB130702A counterpart in rest frame (filled circles), constructed based on our data as well as data from the literature (Singer et al. 2013; D'Elia et al. 2015; Toy et al. 2016). With the exception of the *u* band, which is in actual flux units, all optical and NIR light curves are shifted vertically by increasing powers of 10. The data were *k*-corrected with our spectra (optical filters) and de-absorbed for Galactic extinction with $E(B-V) = 0.037$ mag, using the extinction curve of Cardelli, Clayton & Mathis (1989). The dotted horizontal lines represent the host-galaxy contribution in the various bands; the dot–dashed curves represent the optical afterglow modelled with a steepening power law (see text). The solid curve is the sum of the afterglow and host-galaxy components. The subtraction of these two components from the observed points corresponds to the SN light curves (represented with circles of lighter hue than the observed points in the corresponding band; in *H*-band, the subtraction does not return any positive SN residual signal). The errors on the SN points range from 10 to 15 per cent around maximum to 50 per cent at early epochs, when the contribution of the afterglow is larger. They are not reported for clarity. The black filled circles are the *Swift*/XRT light curve at 1 keV; the best-fitting afterglow model at this energy is reported as a grey dashed curve. (b) Same as (a), with SN light curves only, and limited to the bands where the subtraction returns a significant SN signal. With the exception of the *g* band, which is in actual flux units, all light curves are shifted vertically by increasing powers of 10.

assumptions on the afterglow behaviour and subtraction methods and the slightly different wavelength ranges and cosmologies that were adopted.

We compared the light curve of SN 2013dx with that of SN 1998bw, which is better sampled in the NUV and NIR (Galama et al. 1998; Patat et al. 2001). First, we compared the light curves of both SNe in the range of 4500–8500 Å (constructed as described above), where they are both well observed: these light curves match well near maximum (Fig. 3), although they deviate thereafter, presumably owing to the larger ejecta mass of SN 1998bw, but also possibly because of the presence of a high-density inner core in the ejecta of SN 1998bw (Maeda et al. 2003). Then we compared the light curves of the two SNe computed over the same wavelength range, 4500–10 500 Å, which is the range over which SN 2013dx has

Downloaded from https://academic.oup.com/mnras/article/505/3/4106/6294487 by Liverpool John Moores University user on 01 November 2022

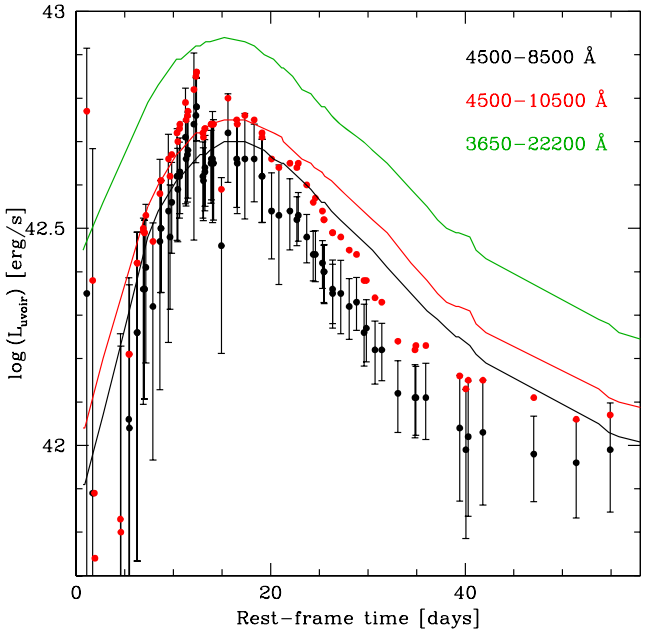

Figure 3. Pseudo-bolometric light curves of SN2013dx integrated over the range 4500–8500 Å (black circles) and 4500–10500 Å (red circles); the uncertainties in the latter points are omitted for clarity. The initial points carry a large uncertainty and do not support any significant claim for the presence of an extra component (e.g. shock–breakout). For comparison, the light curves of SN 1998bw computed in the same ranges are shown as solid curves with the same respective colours, as is the light curve of SN 1998bw computed over the range of 3650–22200 Å (green curve). The data of SN 1998bw were corrected for Galactic extinction $E(B-V) = 0.052$ mags; a distance of 35.1 Mpc was assumed.

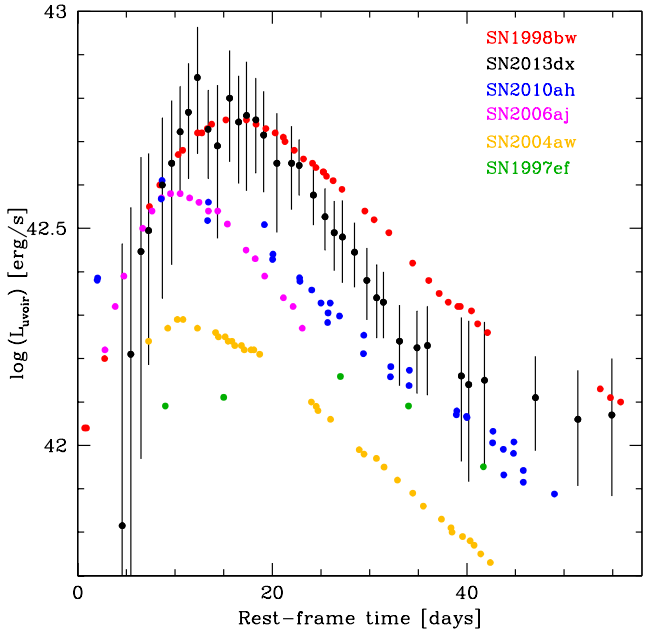

Figure 4. Pseudo-bolometric light curves of well-observed stripped-envelope core-collapse SNe, including GRB-SNe 1998bw (Galama et al. 1998), and SN2013dx, XRF-SN 2006aj (Ferrero 2006; Pian et al. 2006), and SNe 1997ef, 2004aw and 2010ah, all broad-lined SNe that were not accompanied by GRBs (Iwamoto et al. 2000; Mazzali et al. 2013, 2017). The light curves were computed in the same wavelength range (4500–10 500 Å), with the exception of SN 1997ef, which was observed only in the *V* band. For clarity, errors are reported only for SN2013dx. Data of SN 2013dx earlier than 4 d are omitted as they are affected by a large uncertainty (see Fig. 3), while the data that are shown have been binned so that only one data point per day is shown.

the best coverage. The match is still very good, which underlines the similarity of the two SNe and justifies using SN 1998bw as a comparison template for SN 2013dx. The light curve of SN 1998bw in the full range of coverage, 3650–22 200 Å, differs by 0.18 dex from that in the range of 4500–10 500 Å.

A comparison of SN 2013dx with various broad-lined Ic SNe both accompanied and not accompanied by high-energy transients shows that SNe Ic with different properties can exhibit broad light curves (Fig. 4). However, GRB/SNe (2013dx and 1998bw in this figure) have larger luminosities.

Finally, in order to isolate the SN spectra, we subtracted the modelled synchrotron optical afterglow and the host galaxy template spectrum from the observed VLT spectra, corrected for Galactic extinction. The final decomposed spectra are presented in the next section.

3 SPECTRAL MODELLING

The results presented in D'Elia et al. (2015) were based on a simple approximation (Arnett 1982). In particular, they were reliant on approximate measurements of the ejecta velocity as estimated from the position of a very weak line that was identified as Si II 6347, 6371. However, because of line blending, and the quality of the spectra (see fig. 3 in D'Elia et al. 2015), this velocity is very difficult to measure, and the results based on it are consequently highly uncertain. Additionally, a line such as Si II 6347, 6371, which is intrinsically strong, may form well above the pseudo-photosphere, as is well known (see e.g. Mazzali et al. 2000). Given the unexpected spectral properties of SN 2013dx, it is interesting to make an attempt to determine the main parameters of the SN more accurately than previously done, using a more complex and physical approach. Therefore, here we use a full spectral modelling, which allows us to estimate the photospheric velocity $v_{\rm ph}$ rather than just the line velocity.

We followed the procedure we often adopted before when modelling SN data. We used our Monte Carlo radiation transport code for SNe, which is based on the principles outlined in Mazzali & Lucy (1993), Lucy (1999), Mazzali et al. (2000). The code uses the Schuster–Schwarzschild approximation, assuming that the SN luminosity is emitted with a blackbody spectrum from the surface of a pseudo-photosphere whose position moves inwards in mass coordinates with time as the ejecta expand and thin out. Energy packets – which are representative of photons – are injected into the SN envelope, and their propagation is tracked using a Monte Carlo scheme. Packets can interact with the gas in the SN envelope via line absorption or electron scattering. In the case of line absorption, the excited electron is allowed to de-excite through a number of randomly selected allowed downward paths, such that new photons of different wavelength can be emitted. This automatically takes into account the process of line branching, which is essential for the formation of SN spectra (Mazzali et al. 2000). Electron scattering, on the other hand, simply causes a packet to change its direction of travel. However, by doing so, it increases the residence time of energy packets in the SN ejecta, thereby increasing also the probability of line absorption. Radiative equilibrium is enforced, as none of the interactions that are considered results in the loss or gain of energy by the gas or the radiation field when a sufficiently large

Downloaded from https://academic.oup.com/mnras/article/505/3/4106/6294487 by Liverpool John Moores University user on 01 November 2022

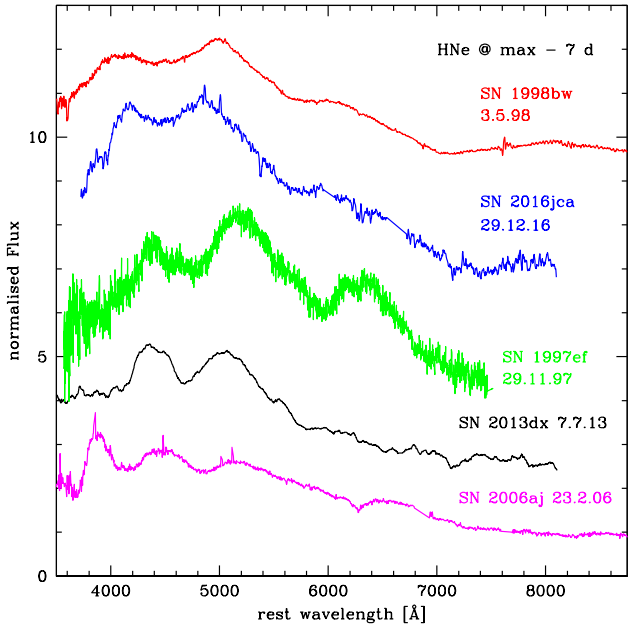

Figure 5. The spectrum of SN 2013dx taken ≈1 week before maximum light compared to those of other broad-lined SNe Ic, both with and without a GRB, obtained at a similar epoch.

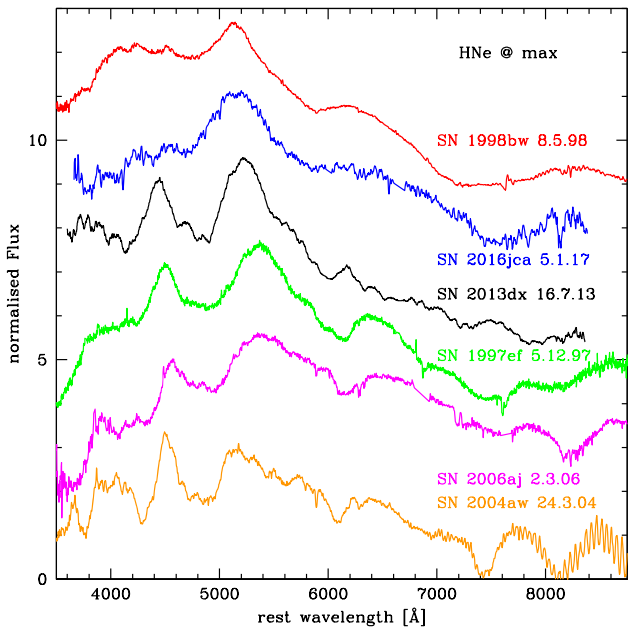

Figure 6. The spectrum of SN 2013dx taken close to maximum light compared to those of other broad-lined SNe Ic, both with and without a GRB, obtained at a similar epoch.

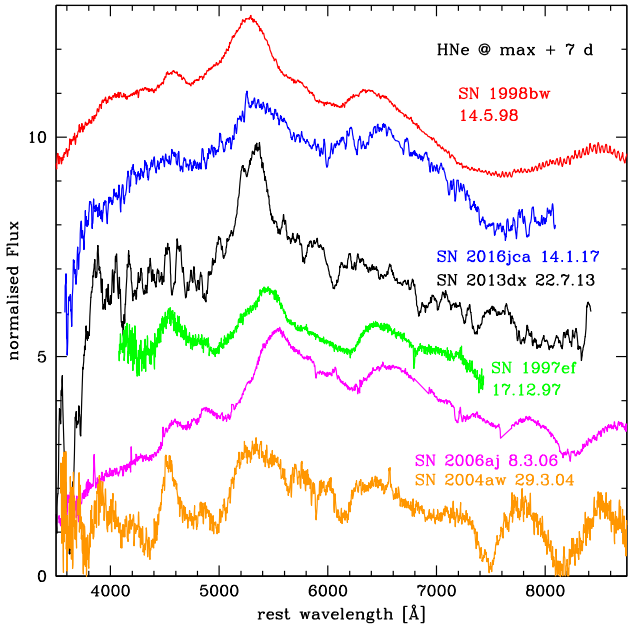

Figure 7. The spectrum of SN 2013dx taken ≈1 week after maximum light compared to those of other broad-lined SNe Ic, both with and without a GRB, obtained at a similar epoch.

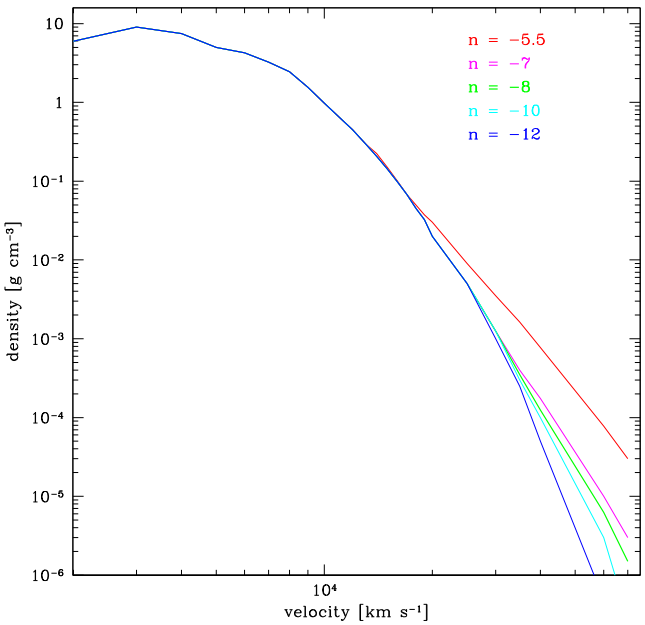

Figure 8. The various density distributions that were tested to match the spectra of SN 2013dx. The values of the density refer to an epoch of 100 s after explosion.

number of interactions are taken into account. Deviation from local thermodynamic equilibrium (LTE) in the low-density, radiation-filled environment of the SN envelope is taken into account by adopting the nebular approximation (Abbott & Lucy 1985; Mazzali & Lucy 1993) for the level population and ionization. This approximation is known to be in excellent agreement with detailed results of a fully non-LTE (nLTE) code (Pauldrach et al. 1996). After the last scattering event, packets that escape are binned according to their frequency in a Monte Carlo spectrum, which is characterized by noise because of the method adopted. A more accurate spectrum can be obtained if a post-iteration is performed when emissivities are computed based on the final occupation numbers, and the formal integral solution of the transfer equation is performed. These are the spectra that are shown here.

The Monte Carlo code requires as input the emerging SN luminosity L, a photospheric velocity $v_{\rm ph}$, and a time from explosion t, from which a photospheric radius is computed. Density in an SN decreases with radius, depending on the properties of the progenitor

Downloaded from https://academic.oup.com/mnras/article/505/3/4106/6294487 by Liverpool John Moores University user on 01 November 2022

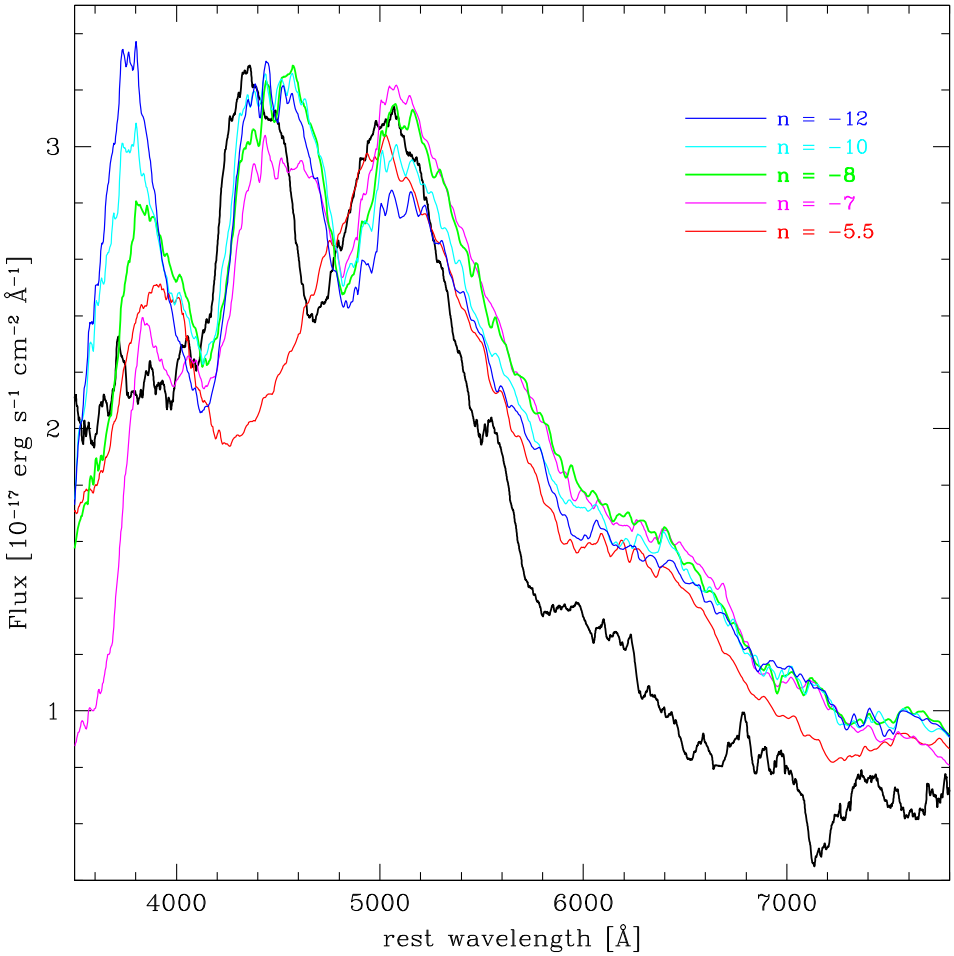

Figure 9. The earliest spectrum of SN 2013dx, obtained on 2013 July 9 at an epoch of 7 d, compared to synthetic spectra computed using the various density distributions shown in Fig. 8.

star and the energy of the explosion. Thus, a density distribution with radius, a so-called explosion model, has to be used, which allows the homologously expanding ejecta to be re-mapped in density to the time that is required for the spectral calculation. Abundances are also a function of radius. In our code, they can be modified as required to optimize the fit to the spectrum. Our code has been applied to different types of SNe. In Mazzali et al. (2008b) we discussed how errors on different quantities can be estimated. This requires looking at the impact that changing each quantity has on the highly non-linear problem that we are solving. In Ashall et al. (2019), we discussed how a broad-lined SN Ic can be analysed and how information can be extracted from the data and the fits, including indirect information about the three-dimensional distribution of the ejecta and the abundances within them, if sufficiently early spectra are available.

The ejected mass $M_{\rm ej}$ and the explosion kinetic energy $E_{\rm K}$ of well-studied GRB–SNe have so far clustered around values of $\sim$10 M$_\odot$ and 3×10^{52} erg, respectively. The energy refers to the isotropic value, which is probably somewhat overestimated, because in GRB/SNe, we are likely to observe the fastest moving ejecta in an aspherical explosion (e.g. Ashall et al. 2019). However, other than the possible requirement of a large progenitor mass, and the hypothesis that the limiting magnetar energy sets an upper limit to the energy, these values are not motivated by any stringent physical argument, unlike, for example, the $M_{\rm ej}$ and $E_{\rm K}$ of SNe Ia. Therefore, selecting a reasonable model is the most important task in a modelling effort, and the most laborious.

The width of the spectral features is normally used as a guideline for the estimate of $E_{\rm K}$, while the shape of the light curve can be used to estimate $M_{\rm ej}$. In this sense, as we already noticed in D'Elia et al. (2015), SN 2013dx resembles spectroscopically energetic SNe Ic that were not accompanied by an observed GRB, such as SNe 2010ah (Mazzali et al. 2013) or 1997ef (Mazzali et al. 2000), rather than any of the well-observed GRB/SNe. We showed in Mazzali et al. (2017) that the slope of the outer density profile directly affects the appearance of the spectra, in particular, the line blending at the earliest times, when line formation occurs in those outermost layers, which by virtue of their high velocity are capable of carrying a significant fraction of the total $E_{\rm K}$. We applied the same methodology here. At the same time, the light curve of SN 2013dx is broader than that of – say – SN 2010ah (see Fig. 4), which indicates a large $M_{\rm ej}$, possibly of the order of 8–10 M$_\odot$.

Given the complexity of establishing a density profile, we started with a detailed comparison of the spectra of SN 2013dx with those of other GRB/SNe as well as broad-lined SNe Ic at various epochs, in order to define a closest analogue. Figs 5–7, show these comparisons at three epochs: $\sim$1 week before maximum, near maximum, and $\sim$1 week after maximum.

Downloaded from https://academic.oup.com/mnras/article/505/3/4106/6294487 by Liverpool John Moores University user on 01 November 2022

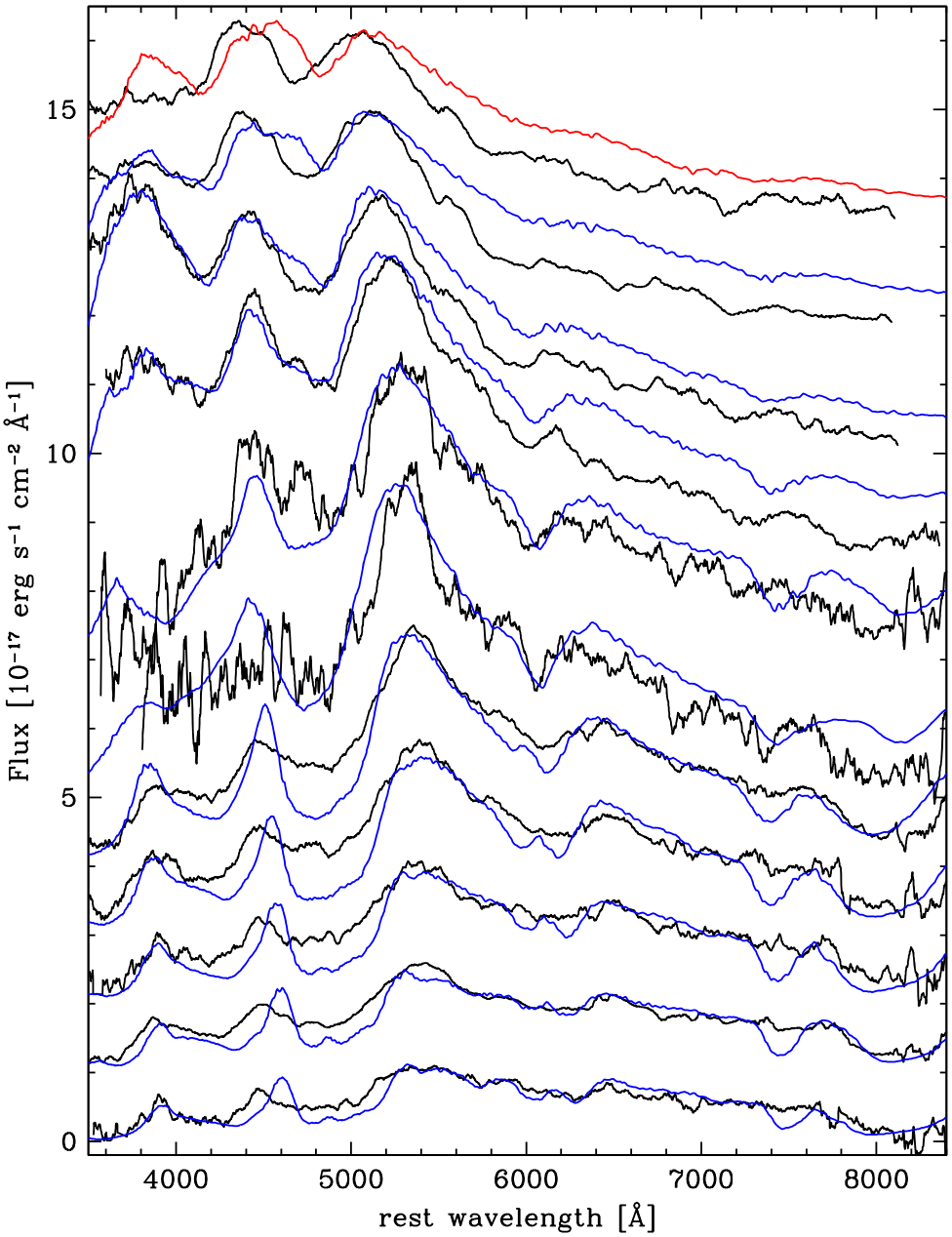

Figure 10. Synthetic spectral fits for the time series of VLT spectra obtained using the density profile with outer density $\rho \propto r^{-8}$. The spectra are displayed from top to bottom in the order shown in Table 1. The flux has been increased by constant values for displaying purposes.

At ∼1 week before maximum (Fig. 5), while the red side of the optical spectrum of SN 2013dx shows similarities to GRB/SNe such as 1998bw and 2016jca, the Fe-dominated absorption near 4800 Å is much deeper and narrower, indicating a smaller velocity and a steeper density profile than in GRB/SNe and even in SN 1997ef. In fact, the spectrum of SN 2013dx is not too different from that of a lower E_K event such as SN 2006aj (Mazzali et al. 2006a; Pian et al. 2006). An estimate of the velocity based on the position of the Si II 6347, 6371 Å line in D'Elia et al. (2015) yielded a high velocity (26 000 km s^{-1}) at this epoch, but it must be noted that the line most probably forms above the pseudo-photosphere, such that comparing directly measured line velocities and photospheric velocities obtained from modelling may be misleading.

The differences are even clearer at maximum (Fig. 6), when a larger sample is available for comparison. SN 2013dx looks spectroscopically quite similar to SN 1997ef and not at all like GRB/SNe 1998bw or 2016jca. The XRF/SN 2006aj is also a good match, as is the moderately energetic SN 2004aw. All of these SNe are characterized by significantly less line blanketing than the GRB/SNe, and the similarity suggests that moderate line blanketing characterizes also SN 2013dx. However, because of the relatively high redshift, the red side of the spectrum of SN 2013dx is not well observed. This is a region where blending of the Ca II IR triplet into the O I 7774 line is a clear indicator of high-velocity ejecta and hence of a high E_K, so we should be careful. A possible Si II 6347, 6371 Å line indicates a velocity of ≈16 700 km s^{-1}, which is significantly less than the 20 000 km s^{-1} reported by D'Elia et al. (2015). The

Downloaded from https://academic.oup.com/mnras/article/505/3/4106/6294487 by Liverpool John Moores University user on 01 November 2022

velocity may actually be even lower if the emission near 6100 Å is spurious, as it may well be given the behaviour of the other SNe in the comparison, which do not show much red emission in the Si II line. The observed spectra point to a significant difference in E_K between SN 2013dx and classical GRB/SNe.

Finally, the spectrum at ≈1 week after maximum (Fig. 7) reflects the dimming of the source and really shows only a peak near 5200 Å. Additionally, the spectrum has a very low signal-to-noise ratio, such that it is practically impossible to see an Si II line, let alone use spectral features to estimate an expansion velocity. The measurement published in D'Elia et al. (2015) is therefore likely to be highly uncertain.

Given these uncertainties, we tested a number of different density profiles, characterized by a similar inner density (and therefore mass) but by different density slopes at high velocity. Based on the procedure followed in Mazzali et al. (2017), we developed density profiles with different gradients in the outer regions. We used as a starting point a model very similar to the one used for SN 1998bw (Iwamoto et al. 1998), except that we reduced the mass to 9 $M_\odot$ and, accordingly, the energy to $\approx 1.4 \times 10^{52}$ erg, in line with the expected mass of SN 2013dx. The outer density in this model behaves like a power law with index $n \approx -5.5$ with respect to radius. The flat slope was required in order to produce the broad lines seen in SN 1998bw. As SN 2013dx has narrower lines, we constructed models with progressively steeper outer density profiles, i.e. $n \approx -7$, -8, -10, and -12. These density profiles are shown in Fig. 8. While the ejected mass does not change significantly in the various models, the value of E_K decreases to 9.5×10^{51}, 9.3×10^{51}, 9.0×10^{51}, and 8.7×10^{51} erg, respectively.

We then computed a series of synthetic spectra for each of our density profiles. For each epoch, we searched for the best convergence based on our choice of L, v_{ph} and the abundances. Because of the different radial dependencies of density, models using different density profiles yield somewhat different values of best-fitting v_{ph}. The luminosity, on the other hand, changes very little from model to model, as it mostly determines the level of the observed flux. As for the abundances, we started with the fiducial values that we used for the outer layers of SN 1998bw (Iwamoto et al. 1998). The initial composition in that case was dominated by oxygen (≈85 per cent by mass), followed by neon (≈10 per cent), carbon (≈2 per cent), silicon (≈1 per cent), and nickel (≈1 per cent). In computing the models, we could fortunately fix the value of t, which greatly helps defining the other parameters.

As the earlier spectra are the most sensitive to the outer density gradient, we show in Fig. 9 a comparison of the synthetic spectra we obtained for the earliest epoch available, 7 d after the GRB. We do see large differences between the steeper and flatter models. In particular, the low-opacity re-emission peak near 4500 Å, which is visible in SN 2013dx but absent in both SN 1998bw and SN 2016jca, is reproduced only in the lower [E_K/M_{ej}] models. Although none of the models shown matches the observed spectrum of SN 2013 perfectly, better matches are provided by models with intermediate values of the slope. Based on the results at this and other epochs, we selected the model with $\rho \propto r^{-8}$ as our fiducial model for SN 2013dx. This model has $E_K = 9.3 \times 10^{51}$ erg.

The synthetic spectrum obtained with that model matches the observed one reasonably well, in particular, with regard to reproducing the re-emission peak near 4400 Å. As Fig. 9 shows, none of the models reproduces the blueshift of the Fe II feature near 4700 Å, and it is difficult to match the flux near 4000 Å, where, however, the data may be uncertain. The density profile we selected offers the best match overall.

Table 1. Model parameters for the synthetic spectra. The uncertainties on the input parameters can be assumed to be similar to those derived in Ashall & Mazzali (2020). Following afterglow and host galaxy subtraction, the uncertainty on an individual value of L and v_{ph} is ∼5 %. However, only a specific combination of L and v_{ph} can produce the correct spectral shape and flux, demonstrating that in practice the errors are much smaller than 5 %, and the input parameters are very well constrained. Furthermore, the error on abundances can be assumed to be less than 25% by mass fraction in each shell (Mazzali et al. 2008b).

Date	t (d)	L (erg/s)	v_{ph} (km/s)	T_{BB} (K)
2013 July 9	7.0	6.03×10^{42}	19 000	8250
2013 July 11	8.7	6.61×10^{42}	17 600	8530
2013 July 13	10.5	8.13×10^{42}	16 300	8550
2013 July 16	13.1	8.32×10^{42}	14 625	8070
2013 July 20	16.6	7.41×10^{42}	13 325	7300
2013 July 22	18.3	7.00×10^{42}	12 550	7070
2013 July 27	22.7	5.69×10^{42}	11 300	6360
2013 July 30	25.4	4.90×10^{42}	10 525	6000
2013 August 3	28.8	4.03×10^{42}	9350	5700
2013 August 6	31.5	3.27×10^{42}	8475	5440
2013 August 10	35.0	2.09×10^{42}	7100	5240

Having now selected a favoured model, we proceeded with modelling the time series of VLT spectra. We performed modelling for all density profiles, but here we show only the results for the profile we selected (Fig. 10). In computing the models, we evolved the density to the appropriate time, used the best-fitting values of L and v_{ph} (see values in Table 1), and adapted the abundances to optimize the fit. The abundances did not change much as a function of depth, although we did see a slightly decreasing abundance of ^{56}Ni with decreasing radius, which confirms that a higher fraction of ^{56}Ni can be located at high velocities near the direction of the jet, because of the combination of abundance and area sampled (see Ashall et al. 2019). Overall, the dominant element in the outer layers of the ejecta that are sampled by the spectra is oxygen (≈75 per cent by mass), followed by neon (≈14 per cent), nickel (≈5 per cent), iron (≈2 per cent), and silicon (≈1 per cent). The synthetic spectra reproduce the observed spectral evolution reasonably well, including line broadening. As time progresses and the degree of ionization decreases, the mismatch in the Fe II trough near 4700 Å disappears. This is a consequence of the lower ionization, which means that the Fe II lines become stronger, while at the earliest epochs, Fe III is more dominant and the Fe II lines form only at very high velocities, such that they actually contribute to the next absorption feature, near 4200 Å. The Si II 6355 line becomes stronger with time as the degree of ionization decreases. The Ca II IR triplet is isolated from the O I 7774 line, but the feature is weak and falls partly outside of the spectral region available because of the redshift of SN 2013dx, so that the calcium abundance is not easy to determine.

The model we selected has $M_{ej} = 9\,M_\odot$ and $E_K = 9 \times 10^{51}$ erg. Of course, our results are approximate. The neighbouring models that we tested give a sense of the effect E_K has on the spectra. We therefore conservatively estimate that $M_{ej} = 9 \pm 2\,M_\odot$ and $E_K = 9 \pm 2 \times 10^{51}$ erg.

4 LIGHT-CURVE MODEL

Having selected a plausible explosion model, one way to verify that it is viable is to use it to compute a synthetic light curve and test it against the observed one.

Downloaded from https://academic.oup.com/mnras/article/505/3/4106/6294487 by Liverpool John Moores University user on 01 November 2022

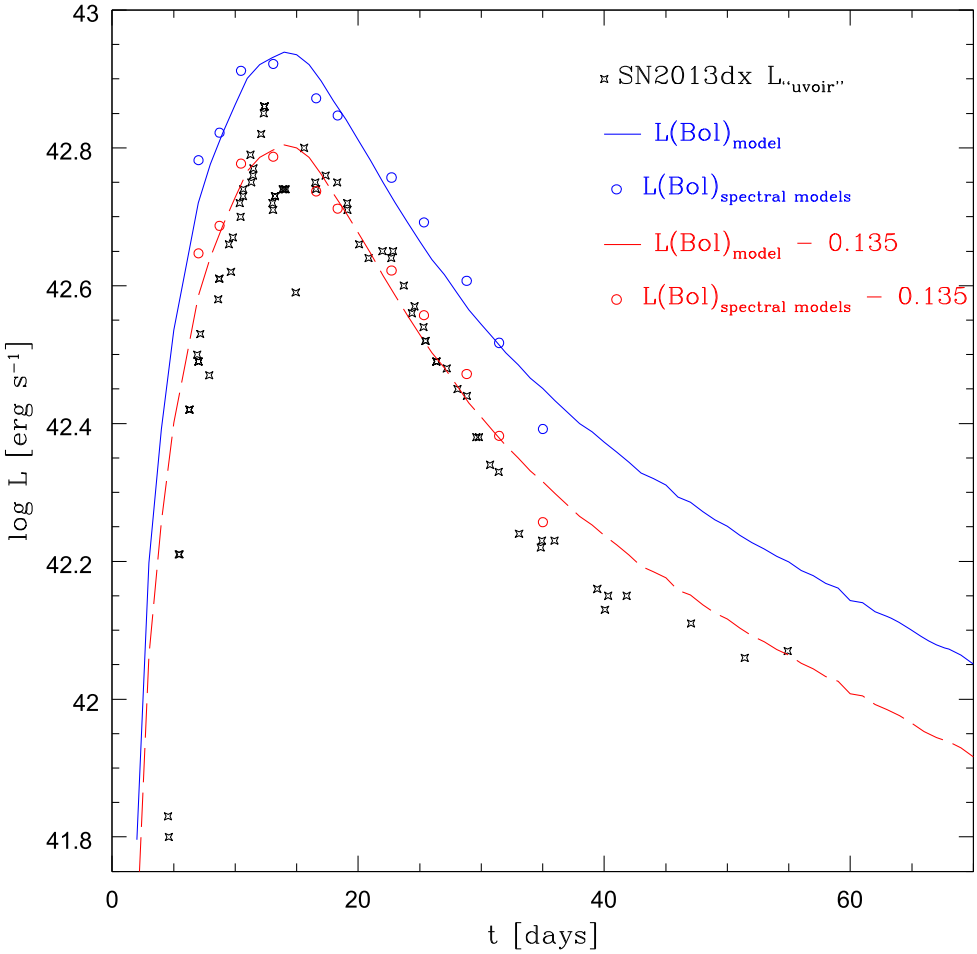

Figure 11. The synthetic bolometric light curve obtained using the density profile and abundances derived from our modelling (blue line), compared to the pseudo-bolometric light curve of SN 2013dx computed in the interval 4500–10 500 Å (black stars). The luminosities that were used in the spectral models are shown as blue circles. The red dashed line and the red circles are the synthetic bolometric light curve and the luminosities used in the spectral models shifted downwards by 0.135 dex.

Using the density and abundance structures that we determined from spectral modelling, we used our SN Monte Carlo light-curve code to compute a synthetic bolometric light curve. The code was initially presented in Cappellaro et al. (1997) and then further developed and used in Mazzali et al. (2001a) and later papers. Using a radial distribution of abundances and densities in homologously expanding ejecta, the code uses a Monte Carlo method to compute the deposition of gamma-rays and positrons emitted in the radioactive decay chain of ^{56}Ni. Both gamma-rays and positrons are allowed to propagate within the ejecta, where they deposit their energy. Their propagation is subject to opacities $\kappa_\gamma = 0.027\,\mathrm{g\,cm^{-2}}$ for gamma-rays and $\kappa_{e^+} = 7\,\mathrm{g\,cm^{-2}}$ for positrons, respectively. Both gamma-rays and positrons are assumed to deposit their energy in its entirety when they are deemed to have encountered a sufficiently large optical depth in their propagation. The energy thus deposited is converted into optical photon energy. Energy packets that represent optical photons are themselves allowed to propagate within the ejecta and are subject to a scattering opacity whose value is determined based on the abundances within the ejecta (Mazzali et al. 2001a). This approach is based on the assumption that in hydrogen-free ejecta, line opacity is the dominant form of opacity. In order to conserve energy, every absorption process is followed by an emission one, so that photons only change direction and thus experience different travel lengths and times before they finally escape. This transforms the exponential energy input from radioactivity into the typical rising and declining shape of a Type I SN light curve. The code has been used to model the light curves of many Type I SNe, both Ia and Ib/c (e.g. Mazzali et al. 2017; Teffs et al. 2020).

Given that we could not use nebular spectra to determine the properties of the inner ejecta, including densities and abundances, the light-curve modelling is not completely self-consistent. The mass of ^{56}Ni was to some extent a free parameter, which we adjusted in order to optimize the fit. The region of the ejecta that we sampled with the spectral modelling extends down to a velocity of ≈7000 km/s. This includes a mass of $\approx 6\,\mathrm{M_\odot}$, leaving some $3\,\mathrm{M_\odot}$ of the inner ejecta unexplored. Within the sampled mass, we already include some $0.32\,\mathrm{M_\odot}$ of ^{56}Ni, with an abundance distribution that decreases slowly with velocity. In the inner, unsampled part of the ejecta, we fixed the ^{56}Ni fraction to the same low level as in the innermost layers that were sampled, ∼2 per cent. This yields a total ^{56}Ni mass of $0.38\,\mathrm{M_\odot}$ and produces the light curve shown in Fig. 11.

When compared to the computed pseudo-bolometric light curve, the synthetic one lies about 0.135 dex above, which is similar to the difference between the pseudo-bolometric light curve of SN 1998bw computed over the same wavelength range as that of SN 2013dx (4500–10 500 Å) and that computed over the broader range of 3650–

Downloaded from https://academic.oup.com/mnras/article/505/3/4106/6294487 by Liverpool John Moores University user on 01 November 2022

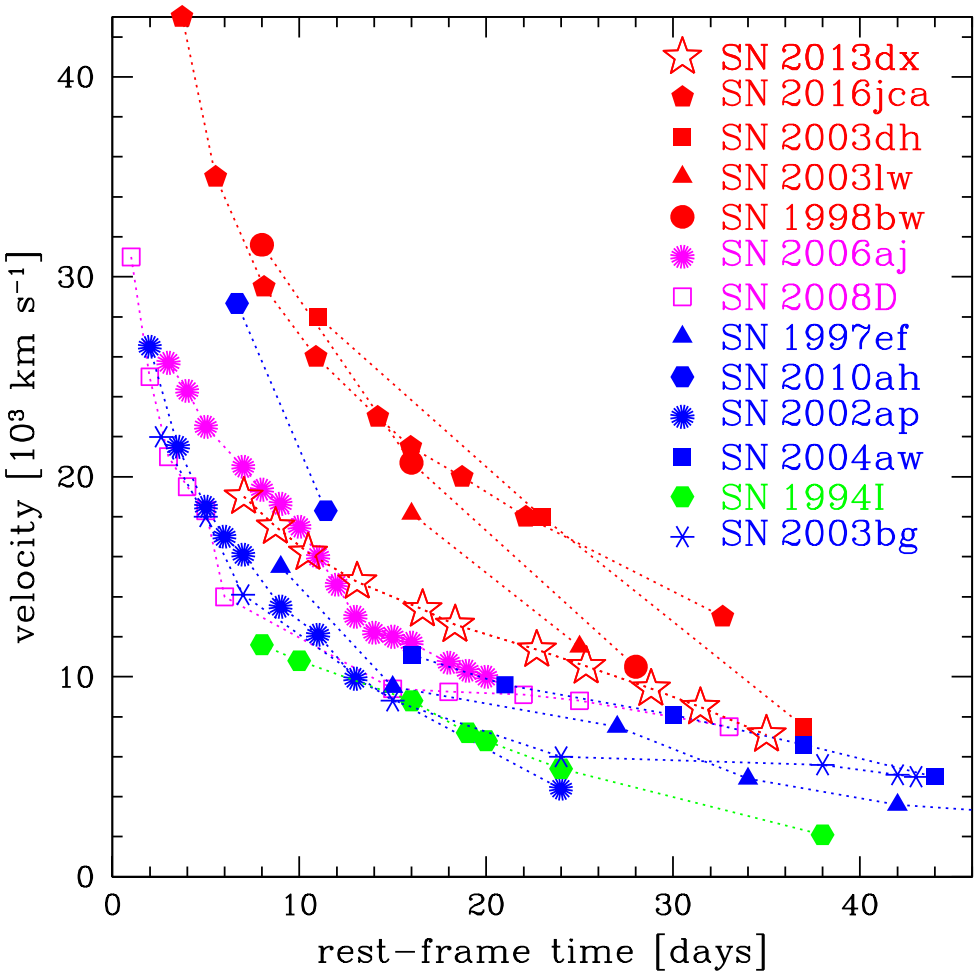

Figure 12. The evolution of the velocity of the pseudo-photosphere as determined by our model spectra for SN 2013dx and a number of broad-lined stripped-envelope SNe.

22 200 Å. This discrepancy is almost certainly due to unobserved near-ultraviolet (NUV) and, especially, NIR contributions, as discussed in Section 2.3. In Fig. 11, we also show the synthetic light curve scaled down by 0.135 dex: the good match between the model and the observations seems to suggest that our estimate of the abundance of ^{56}Ni in the innermost layers is roughly correct. Even if we assumed that no ^{56}Ni is present below 7000 km s^{-1}, the synthetic light curve would still lie above the observed one.

5 DISCUSSION

The properties of SN 2013dx make it quite an unusual GRB/SN. Although it does have broad lines, it is not nearly as broad-lined as the other GRB/SNe. The breadth of the lines is normally associated with the ratio E_K/M_{ej}. In the context of the scheme proposed by Prentice & Mazzali (2018), SN 2013dx would be classified as a SN Ic-4 based upon the number of spectral features in the optical range. GRB/SNe are all Ic-3. The smaller line blending is the result of a lower E_K. We derive for SN 2013dx a value $E_K \approx 10^{52}$ erg. In GRB/SNe, the value of E_K derived from one-dimensional modelling is thought to be overestimated by factors of 2–3 because of the intrinsic asphericity of the explosion (Maeda et al. 2002; Mazzali et al. 2005). As GRB/SNe are viewed on or near the axis of the GRB jet, we also tend to pick up the highest velocity SN ejecta, which may lead to an overestimate of E_K if a one-dimensional analysis is performed. The actual value of E_K for SN 2013dx may therefore be of the order of $3-5 \times 10^{51}$ erg, depending on the actual degree of asphericity of the ejecta. This energy would make SN 2013dx not dissimilar to SNe such as 2004aw or 2010ah. Unfortunately, lack of nebular lines detection makes an estimate of the ejecta asphericity very difficult. Yet, even if the asphericity of SN 2013dx was significantly less than what was inferred in – say – SN 1998bw (Mazzali et al. 2001b), its kinetic energy would be unlikely to be much more than 10^{52} erg.

Based on this information, we can try to place SN 2013dx in the context of other SNe Ic, with and without a GRB. First of all, a carbon–oxygen core mass of $\sim$9 M$_\odot$ is similar to that of other GRB/SNe. Therefore, the progenitor star must have also been similarly massive, probably in the range of 35–50 M$_\odot$. In this sense, SN 2013dx does not constitute an exception, which is reassuring, as a large mass remains an essential factor in causing GRB/SNe.

First, we plot the evolution of the photospheric velocity as derived from our models (Fig. 12). This shows that the v_{ph} of SN 2013dx was always significantly smaller than that of all other GRB/SNe and indeed much closer to several non-GRB broad-lined SNe Ic.

We then show some plots where the main properties of a number of stripped-envelope SNe [M_{ej}, E_K, $M(^{56}\mathrm{Ni})$, M(prog)] are compared to one another (Figs 13–17). We plot only SNe for which the results

Downloaded from https://academic.oup.com/mnras/article/505/3/4106/6294487 by Liverpool John Moores University user on 01 November 2022

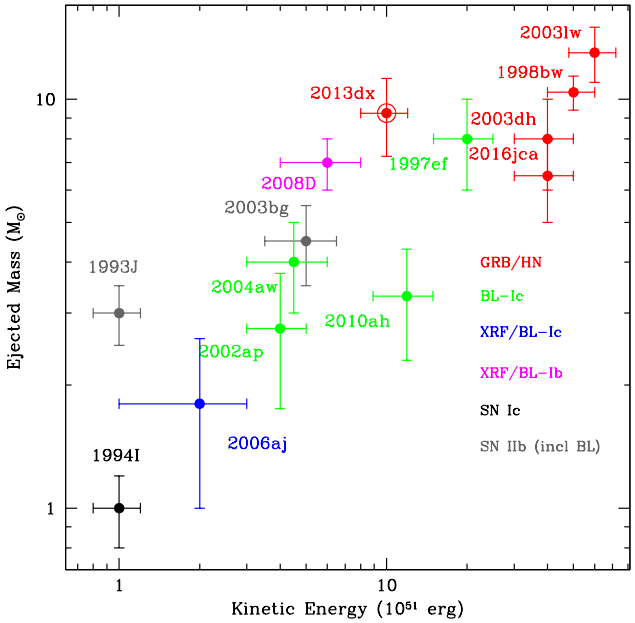

Figure 13. Ejected mass versus kinetic energy in SN 2013dx (highlighted) and in other stripped-envelope SNe. As shown in the figure, red dots indicate GRB/SNe, green dots non-GRB broad-lined SNe Ic, black dots narrow-lined SNe Ic (SN 1994I), blue dots XRF/SNe Ic (SN 2006aj), purple dots XRF/SNe Ib (SN 2008D), and grey dots SNe IIb.

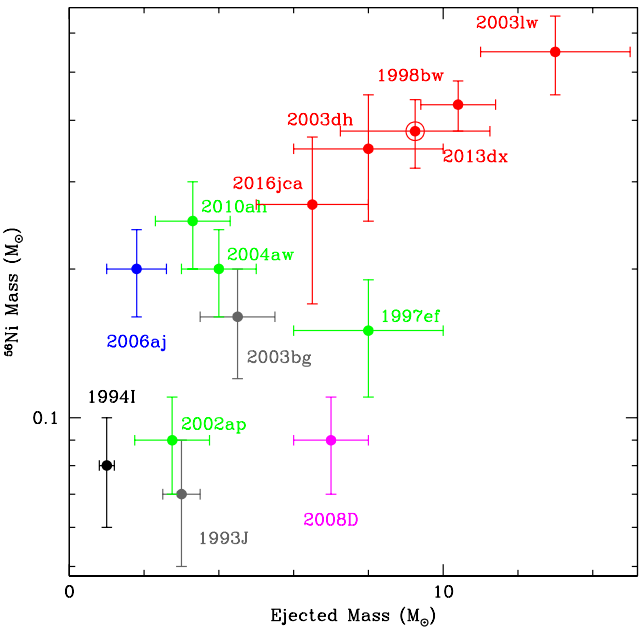

Figure 14. ^{56}Ni mass versus ejected mass in SN 2013dx (highlighted) and in other stripped-envelope SNe. Colour coding as in Fig. 13.

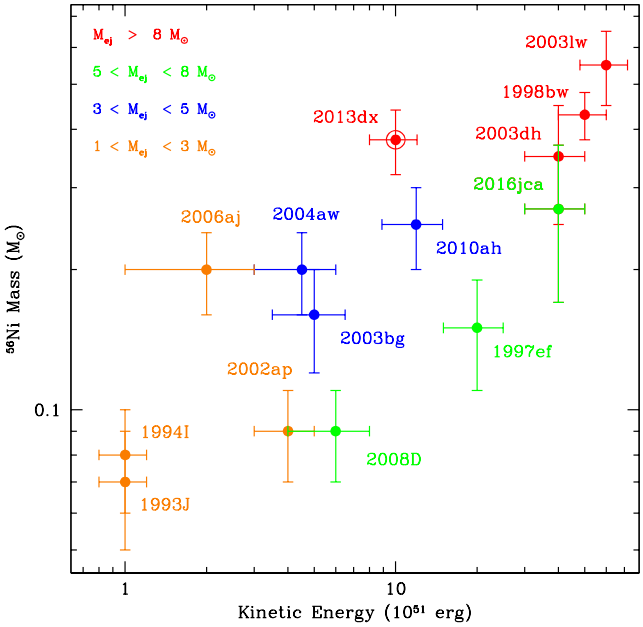

Figure 15. ^{56}Ni mass versus kinetic energy in SN 2013dx (highlighted) and in other stripped-envelope SNe. The colour coding is based on the ejected mass and is explained in the figure legend.

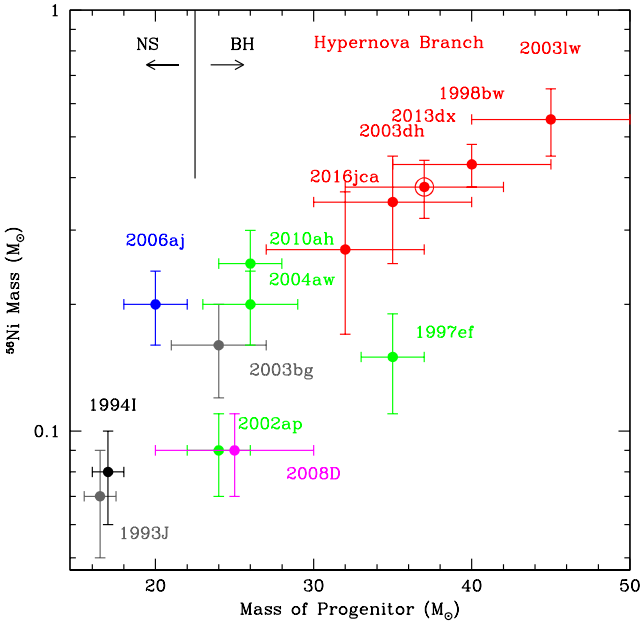

Figure 16. ^{56}Ni mass versus inferred progenitor mass in SN 2013dx (highlighted) and stripped-envelope in other SNe Ic. Colour coding as in Fig. 13.

were obtained with our method, as a simpler approach based on light-curve shape and a single velocity measurement is likely to yield inconsistent results. The position of SN 2013dx is highlighted. While SN 2013dx falls in the group of GRB/SNe in plots that involve $M_{\rm ej}$, M(prog), and $M(^{56}{\rm Ni})$, it is separated from them in terms of $E_{\rm K}$. What is particularly interesting is the plot of $E_{\rm K}$ versus $M(^{56}{\rm Ni})$ (Fig. 15). SN 2013dx synthesized a similar amount of ^{56}Ni as other GRB/SNe but had a much smaller $E_{\rm K}$. This seems to indicate that the relation between $E_{\rm K}$ and $M(^{56}{\rm Ni})$ is not direct. At the same time, if we look at the plots involving $M(^{56}{\rm Ni})$ and either the ejected mass or the inferred progenitor mass (Figs 14 and 16), we see that SN 2013dx falls nicely along the trend that is defined by the other well-studied cases, suggesting that there is a strong correlation between progenitor mass and mass of ^{56}Ni synthesized in the explosion.

The main results we obtained for SN 2013dx are $M(^{56}{\rm Ni}) \approx 0.38\,{\rm M}_{\odot}$, $M_{\rm ej} \approx 9 \pm 2\,{\rm M}_{\odot}$, and $E_{\rm K} \approx 9 \pm 2 \times 10^{51}$ erg. Apart from the ejected mass, which is the parameter that can be obtained most reliably using the width of the light curve, our results differ

Downloaded from https://academic.oup.com/mnras/article/505/3/4106/6294487 by Liverpool John Moores University user on 01 November 2022

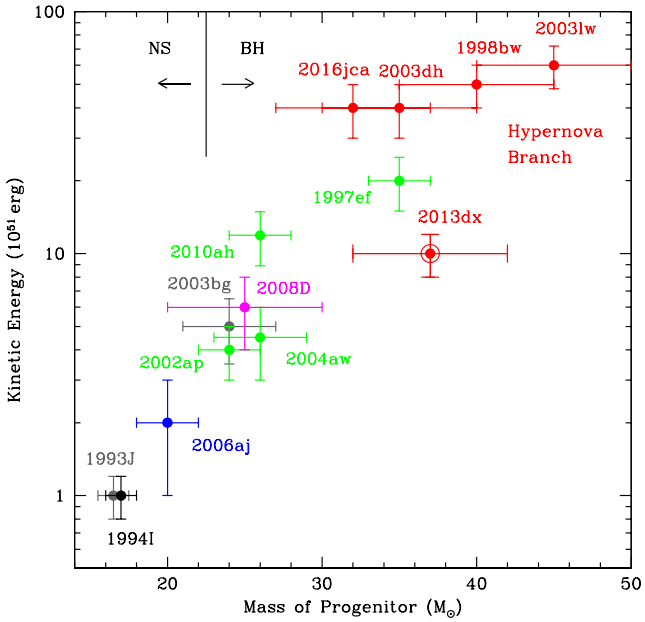

Figure 17. Kinetic energy versus inferred progenitor mass in SN 2013dx (highlighted) and stripped-envelope in other SNe Ic. Colour coding as in Fig. 13.

significantly from those of D'Elia et al. (2015). The difference in the mass of ejected ^{56}Ni can be mostly attributed to our new treatment of the photometry and the bolometric light curve of SN 2013dx. The difference in kinetic energy, for which we find a much lower value, must, however, be ascribed to the fact that D'Elia et al. (2015) used a single measurement of the velocity near light-curve peak, thus missing the fact that at early times the narrower lined character of the spectra indicates a lack of high-velocity ejecta, which actually carry most of the energy in a classical GRB/SN like SN 1998bw.

6 CONCLUSIONS

Mazzali et al. (2014) suggested that the explosion kinetic energy of GRB/SNe (not the light curve, as suggested by Kasen & Bildsten 2010; Woosley 2010) is driven by the energy of a magnetar. The similar luminosity of all GRB/SNe may suggest that $M(^{56}\mathrm{Ni})$ is also related to the energy in a magnetar. It may be that some of the rotational or magnetic energy of the magnetar contributed to the explosion and some to the nucleosynthesis. Nucleosynthesis requires very high densities, so it is possible that when magnetar energy is first released, presumably soon after the end of the collapse phase, just after the proto-NS is formed and before it collapses to a black hole, nucleosynthesis is the first result. Later, as the outer layers of the collapsing star begin to expand and densities drop, magnetar energy can only be used to energize the explosion. While all well-studied GRB/SNe so far reached comparable E_K and produced comparable amounts of ^{56}Ni, SN 2013dx had a smaller E_K. Some possibilities are that initially (in the first fraction of a second, which we may call the 'burning' phase) the proto-NS heated the ejecta causing nucleosynthesis, but that in the later phase, for roughly another second, the 'acceleration' phase, the magnetar ran out of energy to expend on accelerating the ejecta. This may be because it had less energy overall, or it released it more rapidly, or simply that at that point it collapsed to a BH and was no longer able to release energy. It is also interesting that the inner layers are not expected to contain much ^{56}Ni. This may also be a result of different conditions at the time of collapse than in other GRB/SNe.

Clearly, these are just suggestions, but even if they were true, the fact that the GRB was rather normal should also not be very surprising. From a jet break at 3 d, we obtain, for a circum-stellar medium (CSM) density of 1 cm^{-3} and an observed isotropic energy of 6×10^{50} erg (rescaled from the original value reported in Amati et al. 2013, using $H_0 = 73\,\mathrm{km\,s^{-1}\,Mpc^{-1}}$), a jet total opening angle of 20° (Sari, Piran & Halpern 1999), which implies a jet-corrected energy of $\sim 10^{49}$ erg. The jet that causes the GRB would be produced when the proto-NS collapses to a BH, and the conditions for that process would have been no different in SN 2013dx than in other GRB/SNe, so that the energy carried by the GRB is a rather small fraction of the SN kinetic energy also in this case. Certainly, this field is holding many secrets yet, and only continued investigation, both observational and theoretical, can finally reveal them all.

ACKNOWLEDGEMENTS

The late-time observations were performed under ESO programme 092.D-0043(A).

DATA AVAILABILITY

The photometric and spectroscopic data presented in this article are publicly available via the Weizmann Interactive Supernova Data Repository, at https://wiserep.weizmann.ac.il.

REFERENCES

Abbott D. C., Lucy L. B., 1985, ApJ, 288, 679
Amati L., Dichiara S., Frontera F., Guidorzi C., Izzo L., Della Valle M., 2013, GCN Circ., 15025
Arnett W. D., 1982, ApJ, 253, 785
Ashall C., Mazzali P. A., 2020, MNRAS, 492, 5956
Ashall C. et al., 2019, MNRAS, 487, 5824
Bucciantini N., Quataert E., Metzger B. D., Thompson T. A., Arons J., Del Zanna L., 2009, MNRAS, 396, 2038
Cappellaro E., Mazzali P. A., Benetti S., Danziger I. J., Turatto M., Della Valle M., Patat F., 1997, A&A, 328, 203
Cardelli J. A., Clayton G. C., Mathis J. S., 1989, ApJ, 345, 245
Chen K.-J., Moriya T. J., Woosley S., Sukhbold T., Whalen D. J., Suwa J., Bromm V., 2017, ApJ, 839, 85
Dai Z. G., Cheng K. S., 2001, ApJ, 558, L109
D'Elia V. et al., 2015, A&A, 577, A116
Ferrero P., 2006, A&A, 457, 857
Filippenko A. V., 1997, ARA&A, 35, 30
Galama T. J. et al., 1998, Nature, 395, 670
Hjorth J. et al., 2003, Nature, 423, 847
Iwamoto K. et al., 1998, Nature, 395, 672
Iwamoto K. et al., 2000, ApJ, 534, 660
Janka H.-TH., Melson T., Summa A., 2016, Annu. Rev. Nucl. Part. Sci., 66, 341
Kasen D., Bildsten L., 2010, ApJ, 717, 245
Kelly P. L., Filippenko A. V., Fox O. D., Zheng W., Clubb K. I., 2013, ApJ, 775, L5
Kinney A. L., Calzetti D., Bohlin R. C., McQuade K., Storchi-Bergmann T., Schmitt H. R., 1996, ApJ, 467, 38
Levan A., Crowther P., de Grijs R., Langer N., Xu D., Yoon S.-C., 2016, Space Sci. Rev., 202, 33
Lucy L. B., 1999, A&A, 345, 211
Maeda K. et al., 2007, ApJ, 658, L5
Maeda K., Nakamura T., Nomoto K., Mazzali P. A., Patat F., Hachisu I., 2002, ApJ, 565, 405

Downloaded from https://academic.oup.com/mnras/article/505/3/4106/6294487 by Liverpool John Moores University user on 01 November 2022

Maeda K., Mazzali P. A., Deng J., Nomoto K., Yoshii Y., Tomita H., Kobayashi Y., 2003, ApJ, 593, 931
Mazzali P. A. et al., 2003, ApJ, 599, L95
Mazzali P. A. et al., 2005, Science, 308, 1284
Mazzali P. A. et al., 2006a, ApJ, 645, 1323
Mazzali P. A. et al., 2006b, Nature, 442, 1018
Mazzali P. A. et al., 2007, ApJ, 661, 892
Mazzali P. A. et al., 2008a, Science, 321, 1185
Mazzali P. A., 2000, A&A, 363, 705
Mazzali P. A., Lucy L. B., 1993, A&A, 279, 447
Mazzali P. A., Iwamoto K., Nomoto K., 2000, ApJ, 545, 407
Mazzali P. A., Nomoto K., Cappellaro E., Nakamura T., Umeda H., Iwamoto K., 2001a, ApJ, 547, 988
Mazzali P. A., Nomoto K., Patat F., Maeda K., 2001b, ApJ, 559, 1047
Mazzali P. A., Sauer D. N., Pastorello A., Benetti S., Hillebrandt W., 2008b, MNRAS, 386, 1897
Mazzali P. A., Walker E. S., Pian E., Tanaka M., Corsi A., Hattori T., Gal-Yam A., 2013, MNRAS, 432, 2463
Mazzali P. A., McFadyen A. I., Woosley S. E., Pian E., Tanaka M., 2014, MNRAS, 443, 67
Mazzali P. A., Sauer D. N., Pian E., Deng J., Perntice S., Ben Ami S., Taubenberger S., Nomoto K., 2017, MNRAS, 469, 2498
Metzger B. D., Margalit B., Kasen D., Quataert E., 2015, MNRAS, 454, 3311
Modjaz M. et al., 2009, ApJ, 702, 226
Nomoto K., Hashimoto M., 1988, Phys. Rep., 163, 13
Patat F. et al., 2001, ApJ, 555, 900
Pauldrach A. W. A., Duschinger M., Mazzali P. A., Puls J., Lennon M., Miller D. L., 1996, A&A, 312, 525
Pian E. et al., 2006, Nature, 442, 1011
Prentice S., Mazzali P. A., 2018, MNRAS, 469, 2762
Racusin J. L. et al., 2009, ApJ, 698, 43
Riess A. G. et al., 2016, ApJ, 826, 56
Sari R., Piran T., Halpern J., 1999, ApJ, 519, L17
Schlafly E. F., Finkbeiner D. P., 2011, ApJ, 737, 103
Singer L. P. et al., 2013, ApJ, 776, L34
Soderberg A. M. et al., 2008, Nature, 453, 469
Suwa Y., Tominaga N., 2015, MNRAS, 451, 282
Tanaka M. et al., 2009, ApJ, 692, 1131
Teffs J., Ertl T., Mazzali P. A., Hachinger S., Janka H.-T., 2020, MNRAS, 492, 4369
Toy V. L. et al., 2016, ApJ, 818, 79
Uzdensky D. A., MacFadyen A. I., 2007, ApJ, 669, 546
Volnova A. A., Pruzhinskaya M. V., Pozanenko A. S. et al., 2017, MNRAS, 467, 3500
Woosley S. E., 2010, ApJ, 719, L204
Zhang B., Mészáros P., 2004, JIMPA, 15, 2385

This paper has been typeset from a TEX/LATEX file prepared by the author.

Downloaded from https://academic.oup.com/mnras/article/505/3/4106/6294487 by Liverpool John Moores University user on 01 November 2022